GERDA

Progress report to the LNGS scientific committee

(Appendix)

LNGS-EXP 33/05 add. 8/09

This GERDA report summarizes the progress achieved during the last six. It has been written prior to April 6 and the time lines of the various sub-projects do not include delays related to the earthquake which required the suspension of ongoing installation works at the LNGS.

A *Short Write-up* is linked at

`http://www.mpi-hd.mpg.de/GERDA/reportsLNGS/gerda-lngs-sc-apr09-shwup.pdf`.

Experimental and technical details are given in the *Appendix* which is linked at

`http://www.mpi-hd.mpg.de/GERDA/reportsLNGS/gerda-lngs-sc-apr09-appdx.pdf`.

Previous reports are available at `http://www.mpi-hd.mpg.de/GERDA/reportsLNGS`.

April 2009

M. Allardt [c], A.M. Bakalyarov [l], M. Balata [a], I. Barabanov [j], M. Barnabe-Heider [f], L. Baudis [q], C. Bauer [f], E. Bellotti [g,h], S. Belogurov [k,j], S.T. Belyaev [l], A. Bettini [n,o], L. Bezrukov [j], F. Boldrin [n,o], V. Brudanin [d], R. Brugnera [n,o], D. Budjas [f], A. Caldwell [m], C. Cattadori [g,h], E.V. Demidova [k], A. Denisiv [j], A. Di Vacri [a], A. Domula [c], A. D'Andragora [a], V. Egorov [d], A. Ferella [q], F. Froborg [q], N. Frodyma [b], A. Gangapshev [j], A. Garfagnini [n,o], S. Gazzana [a], A. Glück [m], R. Gonzalea de Orduna [e], P. Grabmayr [p], G.Y. Grigoriev [l], K.N. Gusev [l,d], V. Gutentsov [j], A. Hagen [p], W. Hampel [f], M. Heisel [f], G. Heusser [f], W. Hofmann [f], M. Hult [e], L.V. Inzhechik [l], J. Janicsko [m], M. Jelen [m], J. Jochum [p], M. Junker [a], S. Kionanovsky [j], I.V. Kirpichnikov [k], A. Klimenko [d,j], M. Knapp [p], K-T. Knoepfle [f], O. Kochetov [d], V.N. Kornoukhov [k,j], V. Kusminov [j], M. Laubenstein [a], V.I. Lebedev [l], D. Lenz [m], S. Lindemann [f], M. Lindner [f], I. Lippi [o], J. Liu [m], X. Liu [m], B. Lubsandorzhiev [j], B. Majorovits [m], G. Marissens [e], G. Meierhofer [p], I. Nemchenok [d], S. Nisi [a], L. Pandola [a], K. Pelczar [b], F. Potenza [a], A. Pullia [i], S. Riboldi [i], F. Ritter [p], C. Rossi Alvarez [o], R. Santorelli [q], J. Schreiner [f], J. Schubert [m], U. Schwan [f], B. Schwingenheuer [f], S. Schönert [f], M. Shirchenko [l], H. Simgen [f], A. Smolnikov [d,j], L. Stanco [o], F. Stelzer [m], H. Strecker [f], M. Tarka [q], A.V. Tikhomirov [l], C.A. Ur [o], A.A. Vasenko [k], S. Vasiliev [d,j], M. Weber [f], M. Wojcik [b], E. Yanovich [j], S.V. Zhukov [l], F. Zocca [i], K. Zuber [c], and G. Zuzel [f].

[a]) INFN Laboratori Nazionali del Gran Sasso, LNGS, Assergi, Italy
[b]) Institute of Physics, Jagellonian University, Cracow, Poland
[c]) Institut für Kern- und Teilchenphysik, Technische Universität Dresden, Dresden, Germany
[d]) Joint Institute for Nuclear Research, Dubna, Russia
[e]) Institute for Reference Materials and Measurements, Geel, Belgium
[f]) Max Planck Institut für Kernphysik, Heidelberg, Germany
[g]) Dipartimento di Fisica, Università Milano Bicocca, Milano, Italy
[h]) INFN Milano Bicocca, Milano, Italy
[i]) Dipartimento di Fisica, Università degli Studi di Milano e INFN Milano, Milano, Italy
[j]) Institute for Nuclear Research of the Russian Academy of Sciences, Moscow, Russia
[k]) Institute for Theoretical and Experimental Physics, Moscow, Russia
[l]) Russian Research Center Kurchatov Institute, Moscow, Russia
[m]) Max-Planck-Institut für Physik, München, Germany
[n]) Dipartimento di Fisica dell'Università di Padova, Padova, Italy
[o]) INFN Padova, Padova, Italy
[p]) Physikalisches Institut, Eberhard Karls Universität Tübingen, Tübingen, Germany
[q]) Physik Institut der Universität Zürich, Zürich, Switzerland

Spokesperson: S. Schönert,
(Stefan.Schoenert@mpi-hd.mpg.de)
Co-Spokesperson: C. Cattadori
(Carla.Cattadori@lngs.infn.it)
Technical Coordinator: K.T. Knöpfle
(Karl-Tasso.Knoepfle@mpi-hd.mpg.de) URL:
http://www.mpi-hd.mpg.de/GERDA/reportsLNGS

Contents

1 Cryogenic vessel and infrastructure

The final documentation for the cryostat is available since August '08 and its formal certification according to AD2000 has been issued by TÜV Nord on 4th November 2008.

In the course of the hydrostatic test of the water tank (WT) the cryostat was immersed in water for a period of about 2 months. After water drainage, both water tank and cryostat showed clear evidence for corrosion part of which being due to steel debris which had been produced by works on the GERDA platform and which had been fallen into the WT through uncovered flanges on the WT's roof. Other corrosion spots, however, could hardly be attributed to this origin but were caused rather by scratches, carbon steel contamination or insufficient pickling and passivation. Repair of corroded spots was done by a commercial company; in case of the cryostat the procedure included the following steps: grinding, pickling with Avesta 101, and passivation with Avesta FinishOne 630; between pickling and passivation the complete surface of the cryostat was treated with 'Remox'. After this procedure, still about 100 corrosion spots remained; they have been removed subsequently by another repair cycle including more intense grinding.

The cryogenic infrastructure has been manufactured and delivered by the Dutch company DeMaCo. The cryogenic lines running from the LN and LAr storage tanks via the valve box up to the manifold on top of the cryostat's neck have been installed in March '09 (Fig. 1). First cold tests have proven the basic functionality of the setup. With respect

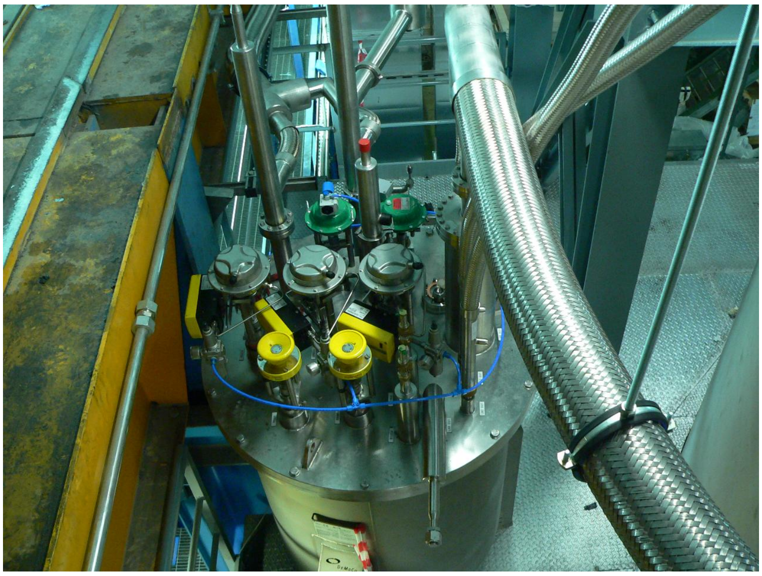

Figure 1: View of valve box and connecting cryogenic lines.

to safety the final Piping & Instrumentation Diagram (PID) shows further improvements as compared to the previous version, see Fig. 4: (i) safety valves PCV021/132 at the exit of both the LN and LAr storage tanks will close automatically the line in case of rupture of the tubing between tank and cryostat, (ii) an additional water cooling circuit for the heater of the exhaust gas that is fed from the water tank via an extra pump. In case of a failure of the LNGS cooling (i.e. heating) water supply, water out of the GERDA water tank will be used for the heat exchanger, and (iii) temperature and differential pressure sensors (TT306/308, DPT305/309) at the exhaust gas heater for improved diagnostic of exhaust gas flow. Based on this final PID a GERDA procedure 'Alarm levels and Corresponding Actions' has been prepared for discussion with the LNGS SPP.

The cryogenic infrastructure will be completed by the installation of the active cooling system, and the tubes leading to the safety valves and exhaust gas heater. The active cooling system will be inserted into the cryostat through its neck. All connections are made with metal-sealed feed-throughs mounted at the manifold. Fig. 2 shows photos of the successful test installation in Heidelberg. While the manifold has been already installed by now, the installation of the active cooling system itself needs a rather large clean environment so that it will be done in the clean room on top of the GERDA experiment which will become operational early in May.

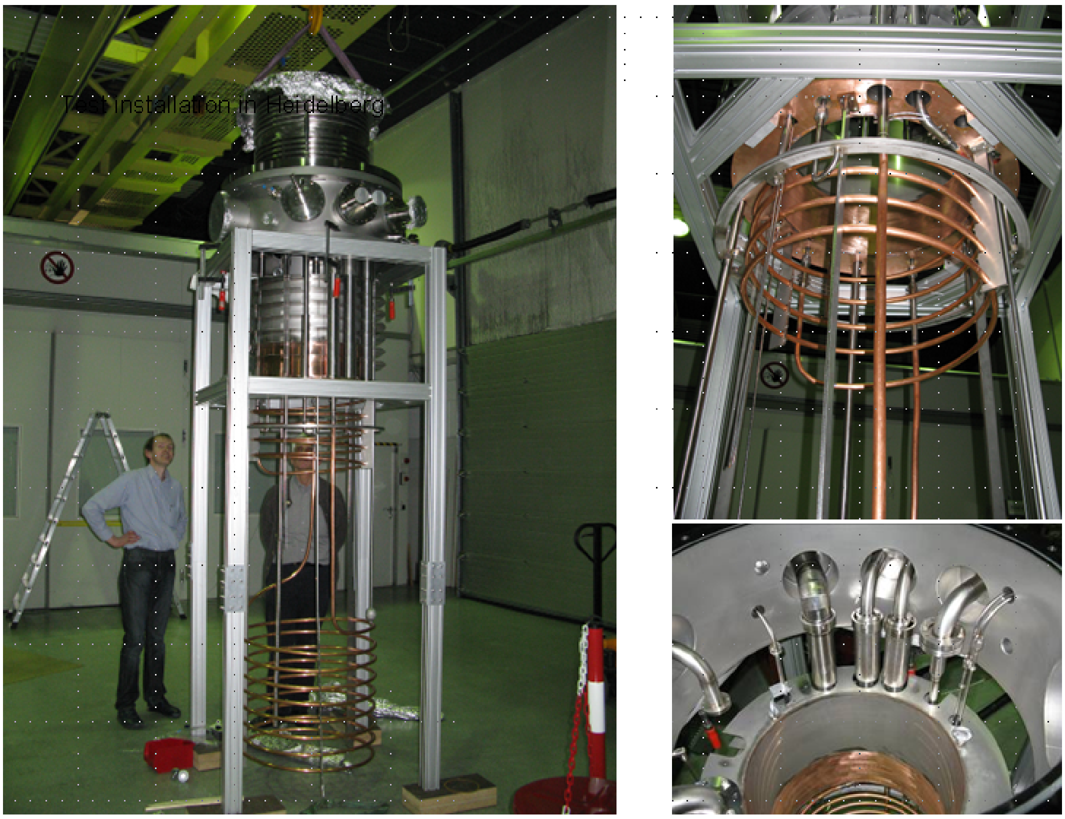

Figure 2: Test installation of active cooling system with manifold in Heidelberg, and views from bottom and top.

In the meantime fabrication and installation of the pipe work connecting cryostat, safety valves and exhaust gas heater is in progress. Fig. 3 shows an assembly drawing of the pipe work at the exhaust gas heater. The PLC controlling the cryogenic infrastructure has been delivered and a first debugging phase has been concluded at Heidelberg. The final commissioning at LNGS is planned for June followed by the filling of the cryostat with LAr.

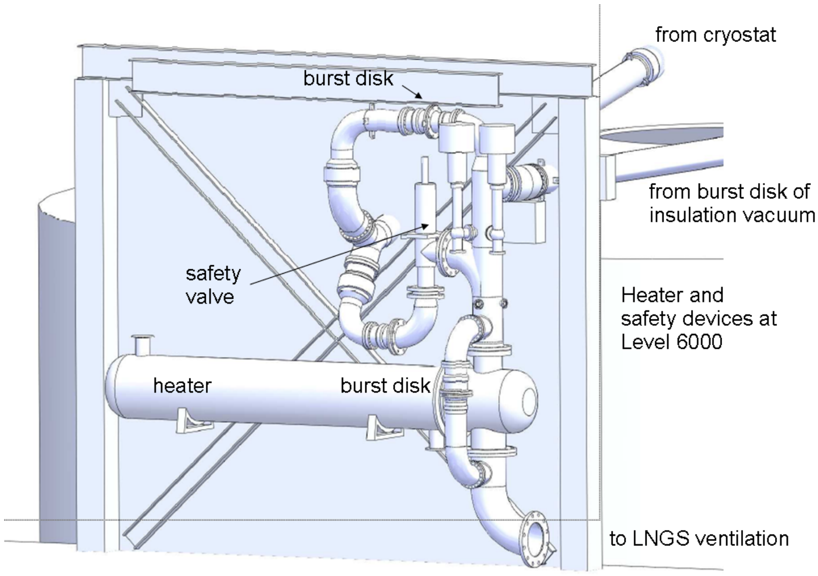

Figure 3: Arrangement of pipes and safety valves at the exhaust gas heater which will be located in a lab room on level 6m. The support structure for the heater is not shown.

After the mounting of the internal copper shield, another measurement with the MOREX appartus showed that the Rn emanation in the cryostat had increased from 14 ± 3 mBq to 34 ± 8 mBq. In a third rather laborious cleaning cycle all accessible surfaces inside the cryostat were wiped with propanol wetted tissues under cleanroom conditions. Unfortunately, this action lowered the Rn emanation only insignificantly to 30 ± 3 mBq. A limit for an acceptable Rn emanation had been deduced earlier by assuming a homogeneous Rn distribution within the cryogenic liquid; in this case 8 mBq would add 10^{-4} cts/(keV·kg·y) to the background index (BI), and the measured value would be far too high. However, this model is now considered to be unrealistic since the strong mixing needed for a homogeneous distribution is improbable in view of the short diffusion length of Rn in LAr, and since the convection inside the cryostat will transport the Rn from the walls to the Ge array. Modeling this latter case we have found [1], however, that the allowed concentration limits for a BI of 10^{-4} cts/(keV·kg·y) must be reduced compared to those for a homogeneous distribution. Instead, by installing a shroud of 800 mm diameter around the detector array, the Rn will be kept far enough from the diodes such that a BI of $< 2{\cdot}10^{-4}$ cts/(keV·kg·y) can be achieved for Phase-I at the measured emanation value of 30 mBq. Installation of the shroud should happen at the same time as the active cooling system once the clean room construction on the GERDA platform is finished (see above). A decision on whether to install the shroud will be taken soon.

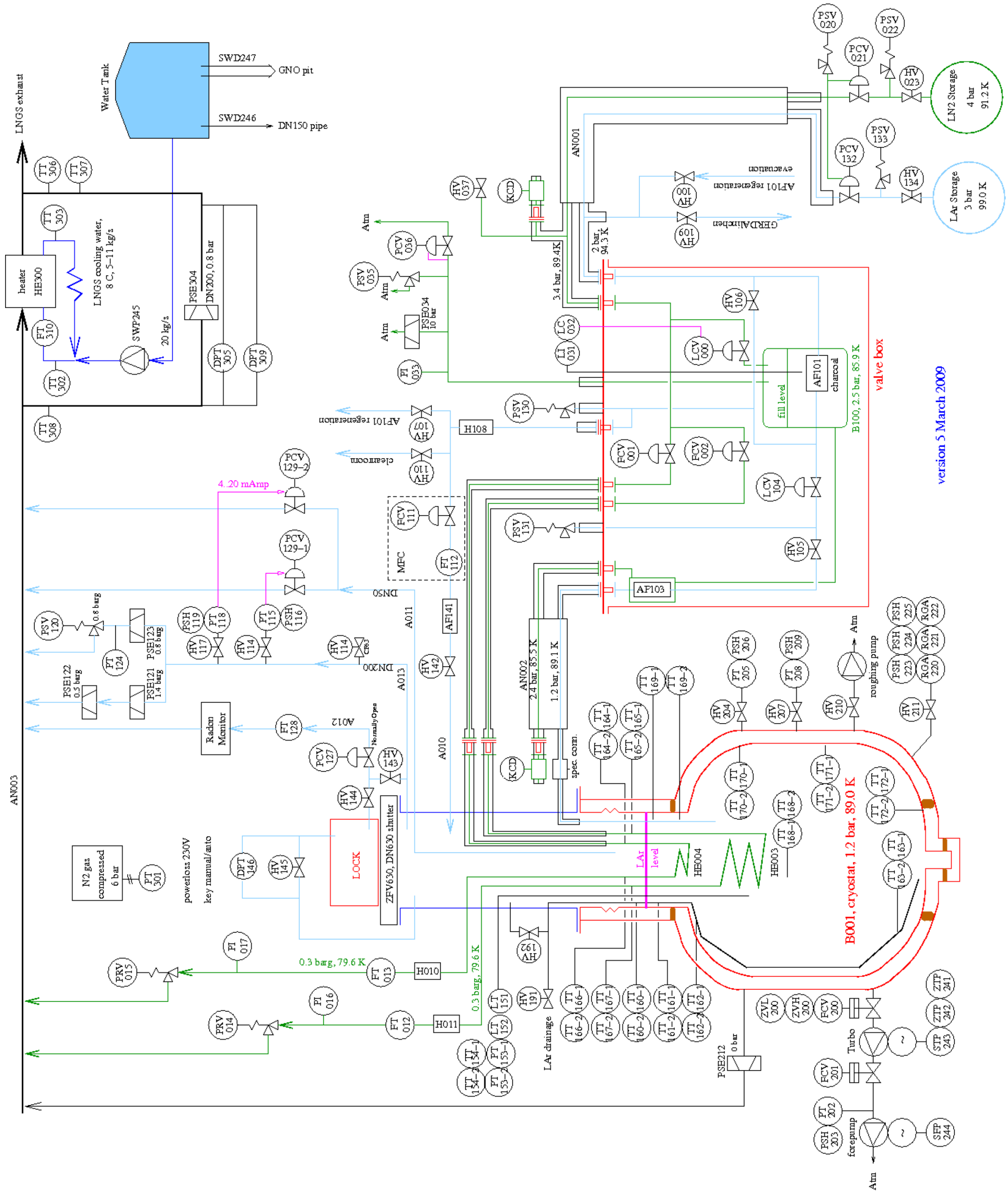

Figure 4: Final Piping and Instrumentation Diagram

2 Water tank and related issues

The water tank (WT) filling for the static test started on November 24, 2008 using the water from the fire-extinguishing loop. No displacement of the cryostat neck during filling of the water tank could be observed. The hydrostatic test consisted of the measurement of the radial deformation of the tank as a function of the water column height, and of an overpressure of 100 mbar after filling. The radial deformations have been measured at the four locations indicated in Fig. 5, three locations (manhole, $+90^0$, $+180^0$) at 1 m height and one location ($+180^0$) at 3 m height.

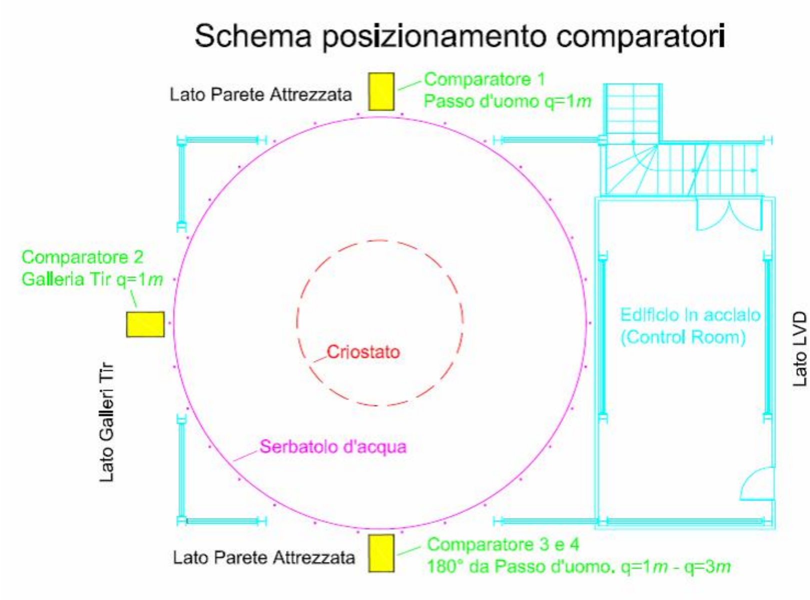

Figure 5: The locations of the instruments that measured the WT radial deformations as a function of the water column height.

The maximal deformations (7-8 mm) have been measured at the manhole site and at the ($+180^0$, 3 m height) locations; the deformations expected by the structural model calculations are also maximal for these two locations. The tank deformations are elastic; in fact the deformations measured while emptying reproduce, with opposite sign, the deformations measured while filling as shown by the black (filling) and red (emptying) curves of Fig. 7.

The fast drain line connecting the tank to the waste water network running below the TIR tunnel has been realized as shown in Fig. 6; the two lines will allow to discharge the water at a flow rate of $\approx$ 60 l/s. The line to bring the demineralized water from the Borexino plant to the GERDA tank as well as the water loop equipped with an Ultra-Q unit to maintain the water clean have been constructed. In February after emptying the tank, at the first inspection it was evident that there was a corrosion problem on the inner surface of the tank and on the outer surface of the cryostat. The corrosion had two origins: first, for an error while managing the work site, the top flanges of the tank were kept open during the construction of the superstructure. A significant quantity of black steel powder entered in the tank through the open flanges and deposited mainly on the horizontal surfaces of the tank (floor) and cryostat (top head). Beside the surface corrosion, several deeper rust points or scratches have been found both on cryostat and tank steel plates. The same repair procedures as for the cryostat have applied, see section 1. The operations took three weeks for diagnosis and definition of procedures and the selection of the company to do the work on-site, and two weeks for the cryostat and WT treatment; on March 23 the tank was finally ready to mount the muon veto system.

Figure 6: The 46 l/s GERDA water drain line. The flow regulator, a completely passive device, is the barely visible blue object in the background.

On March 23rd, the Provincia di Teramo sent the written authorization to LNGS to drain the water coming from the GERDA setup, in the LNGS waste water network both in normal and in emergency operations.

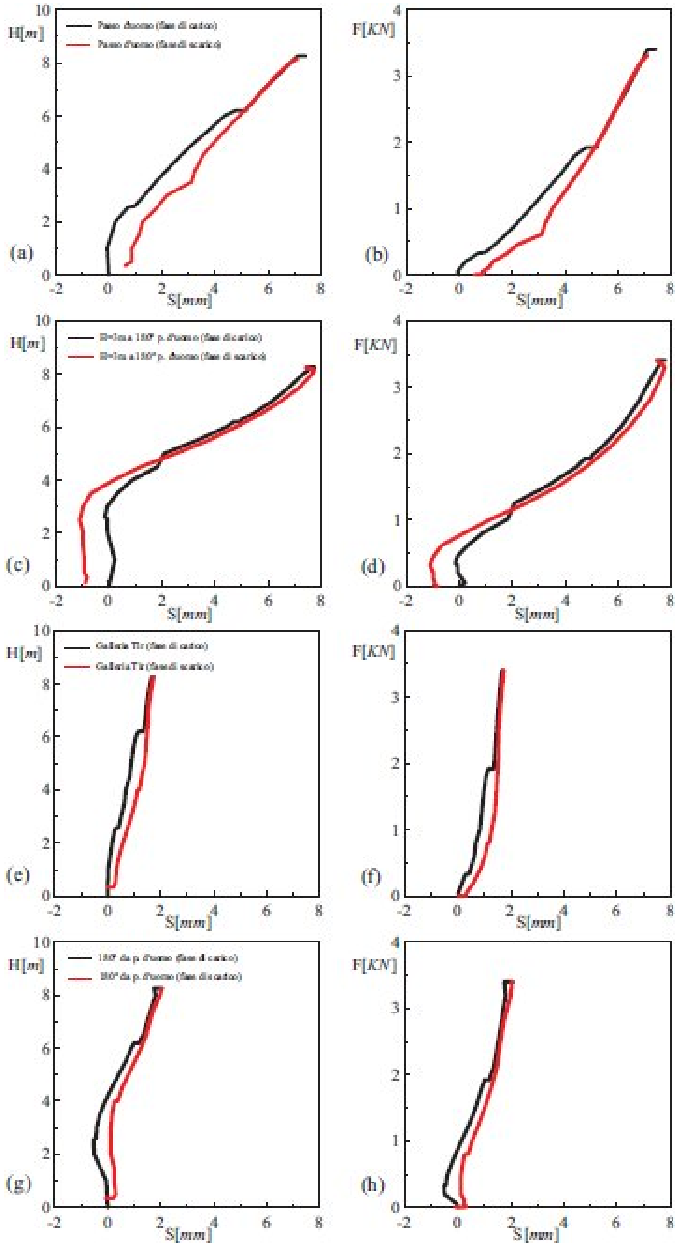

Figure 7: The WT measured radial displacements (x-axis) versus the water level height (y-axis) during filling (black curves) and draining (red curves).

3 Muon veto system

The PMT encapsulations for the Cherenkov Veto have been checked finally before sending them to LNGS. Draining the water after the hydrostatic test of the water tank and the final cleaning of the inside of the water tank and the cryostat, as described in section 1 set the starting point for the installation of the Cherenkov muon veto system inside the water tank to March 23. Presently, the installation of the muon veto is ongoing. In a first step, two personal lifters have been moved inside the water tank in order to access the top region. In clean room conditions, i.e. a tent at the entrance, hepa-filtered air and using clean room suits, the wave length shifting and reflective mirror foil VM2000 is glued to the outer wall. Afterwards the cable trays and the PMT encapsulations are mounted on the wall. When unpacking the capsules the PMT will be tested again. Another performance test will be done after the mounting. The wrapping of the cryostat and the instrumentation of the "pill box" is postponed after the final inspection of the cryostat for corrosion. The capsules will be parked in the water tank and tested. Thus, their final installation is a half-day work and can be done without the lifters. Therefore, the water tank could be water filled for further test without compromising the work on the muon veto.

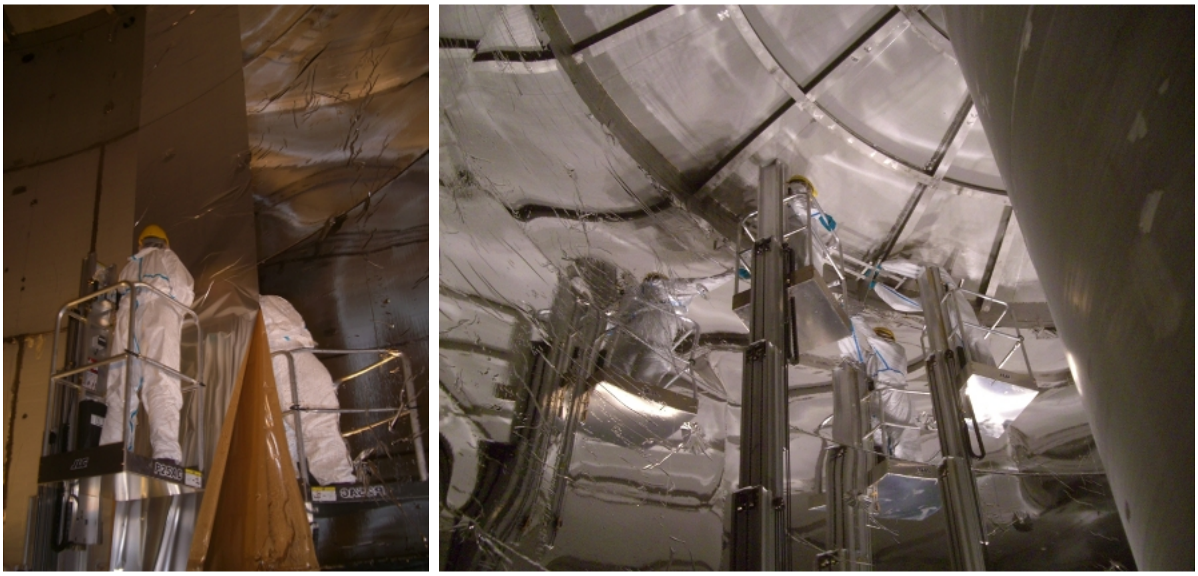

Figure 8: Mounting of the wavelength shifting and reflecting mirror foil inside the water tank.

4 Clean room and lock systems

4.1 Clean room

The Clean Room installation is in its final state of assembly. The steel structure, wall elements, ventilation system as well as electric installations have been completed. Finishing the clean room floor as well as a test run of the clean room are expected for mid April. Approval of the clean room by the GERDA collaboration is scheduled for the 30th of April 2009. In the course of May 2009 the gas system and vacuum infrastructure for the lock system are scheduled to be mounted.

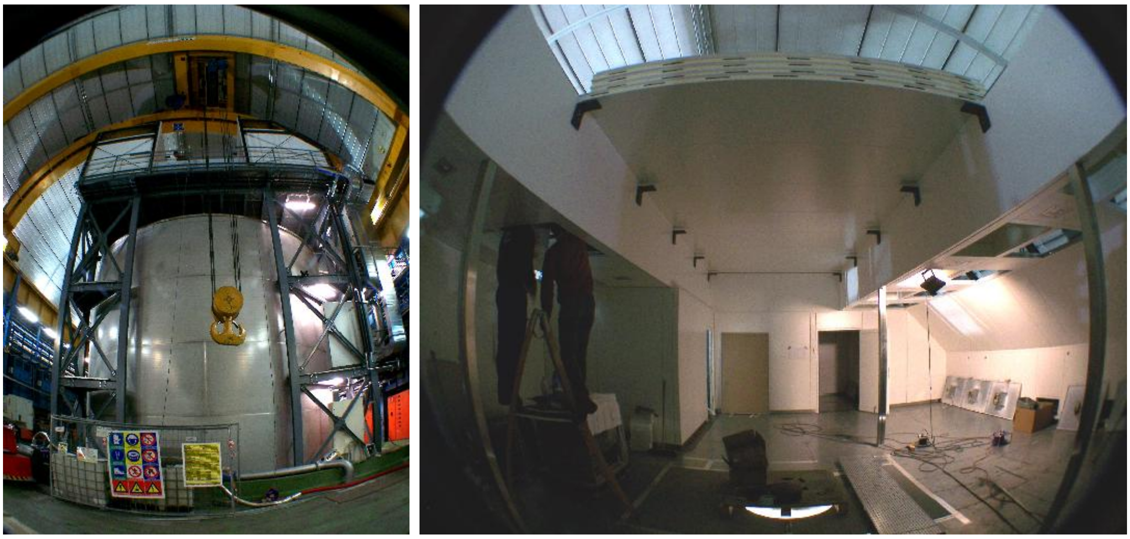

Figure 9: Left: The GERDA water tank with the Clean Room on top. The wall system of the clean room is attached to a steel structure that has been erected onto the superstructure floor. Right: Clean room from inside. The removable roof is half closed with roof segments. The roof will be opened for the lock installation.

4.2 The commissioning lock system

Installation of the temporary commissioning lock system is approaching completion. The two linear pulleys have been fully mounted and are presently tested. Arrival of the commissioning lock system at LNGS is foreseen for the second half of April. Its integration with the glove box in the above–ground Hall di Montaggio will be completed by the end of the month.

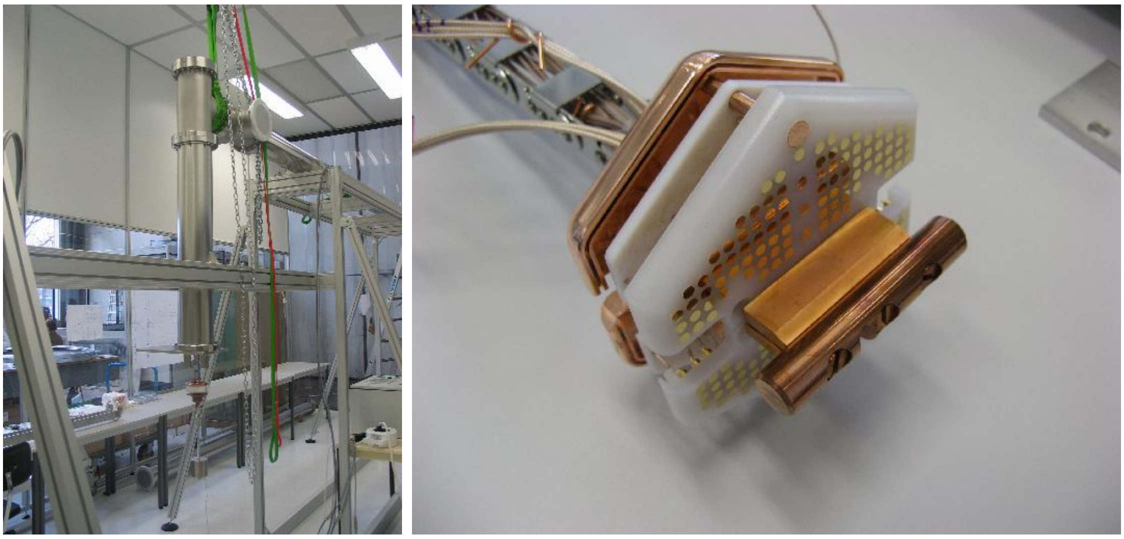

Figure 10: Left: First arm of commissioning lock as assembled in Munich. Right: Connecting matrix installed inside the cable arm. The cabling is already mounted.

4.3 The final lock system

The construction drawings of the final lock system have been completed and are presently at TÜV for approval according to the pressure vessel code AD2000. The tender for the steel cylinder will start in April. Delivery of the cylinder is expected by the end of 2009. Mounting of the linear pulley and the rail systems into the cylinder will start end of 2009. Delivery of the final lock system onto the GERDA cryostat at LNGS is expected for the first half of 2010.

5 GERDA infrastructures at LNGS

The installation of the general infrastructures of GERDA in Hall A is proceeding smoothly. The construction of the GERDA building has been concluded. The electrical plants have been installed and the safety systems are close to completion. Also the installation of the water recirculation plant is in its final phase. The storage tanks for LAr and LN_2 have been placed at the position assigned by LNGS (Fig. 11), and the installation of the cryogenic infrastructure by the DeMaCo company has been concluded.

The work for the installation of the air ducts for the ventilation system connecting GERDA to the LNGS ventilation has started and will be concluded by the end of April. The path of the ventilation had to be modified to comply with the needs of LVD. This caused an uncritical delay in the tendering and, more important, an increase in the budget allocated for the air ducts. As a consequence the integration of the system into the LNGS supervision system for the ventilation had to be removed from the contract and must be tendered separately. The funds for this tender have not yet been allocated by LNGS.

Figure 11: View of the LAr and LN_2 storage tank installation.

For the integration of the commissioning lock with the glove box, the front-end electronics and operation of a Phase I prototype detector string, which will be carried out in the Hall di Montaggio, a platform with a height of 1.80 has been mounted. A clean area enclosed by a tent with hepa-filter ventilation has been installed on top. Electrical power and Ethernet connection are available on the platform.

6 Phase I detectors

After completing the re-processing of Phase I detectors and their testing in the underground Germanium Detector Laboratory (GDL) (WP4), summarized in the last progress report and in Ref. [2], the activities of task group one (TG-1) focused on the preparation of the integration of Phase I detectors with the commissioning lock and the front-end electronics, and on the completion of the low-background test stand LArGe (WP5).

6.1 Phase I integration

Based on the Phase I detector mounting and handling procedures developed during the tests in the GDL, a glove box has been designed and built to enclose and support the commissioning lock. It serves to mount and handle the detectors under hepa-filtered nitrogen atmosphere, to avoid exposure to air, humidity and radon.

The glove box includes mechanical devices to assemble Phase I strings and transfer them into the commissioning lock, as well as a system to warm up the detectors in alcohol after removal from the liquid argon, all under nitrogen atmosphere. A stainless steel dewar with an active cooling system, simulating the cryostat, has been assembled and will be attached below the commissioning lock and glove box. The complete system will be installed in the above-ground Hall di Montaggio of LNGS by the end of April to start the integration phase with non-enriched detectors. The final detector string assembly, commissioning lock, front-end electronics and data acquisition will be tested and debugged in parallel to the liquid argon filling and commissioning of the cryostat underground in Hall A.

6.2 Low-background test stand LArGe

The completion and successful cryogenic tests of the low-background cryostat have been summarized in the last report. The procurement of the vacuum insulated valves and transfer lines for nitrogen cooling and for liquid argon filling of the low-background cryostat has been completed. A slow control system for the LArGe test stand has been setup and tested. It includes the control of the mass flow controller for the active cooling, the reading of the temperature sensors, pressure gauges and the load cells, as well as the control of the high-voltage units for the photo multipliers (PMTs) and germanium detectors.

The low-background voltage dividers have been produced and mounted to the PMTs. After mounting of the cables, feedthroughs and connectors, the PMTs were tested successfully for voltage break downs and discharges in argon gas. The PMTs were subsequently mounted in the final PMT support structure and integrated into the LArGe cryostat. Figure 12 displays the different steps of the PMT integration into the cryostat. Gain calibration and dark noise measurements are currently being carried out inside the cryostat filled with argon gas at ambient temperature.

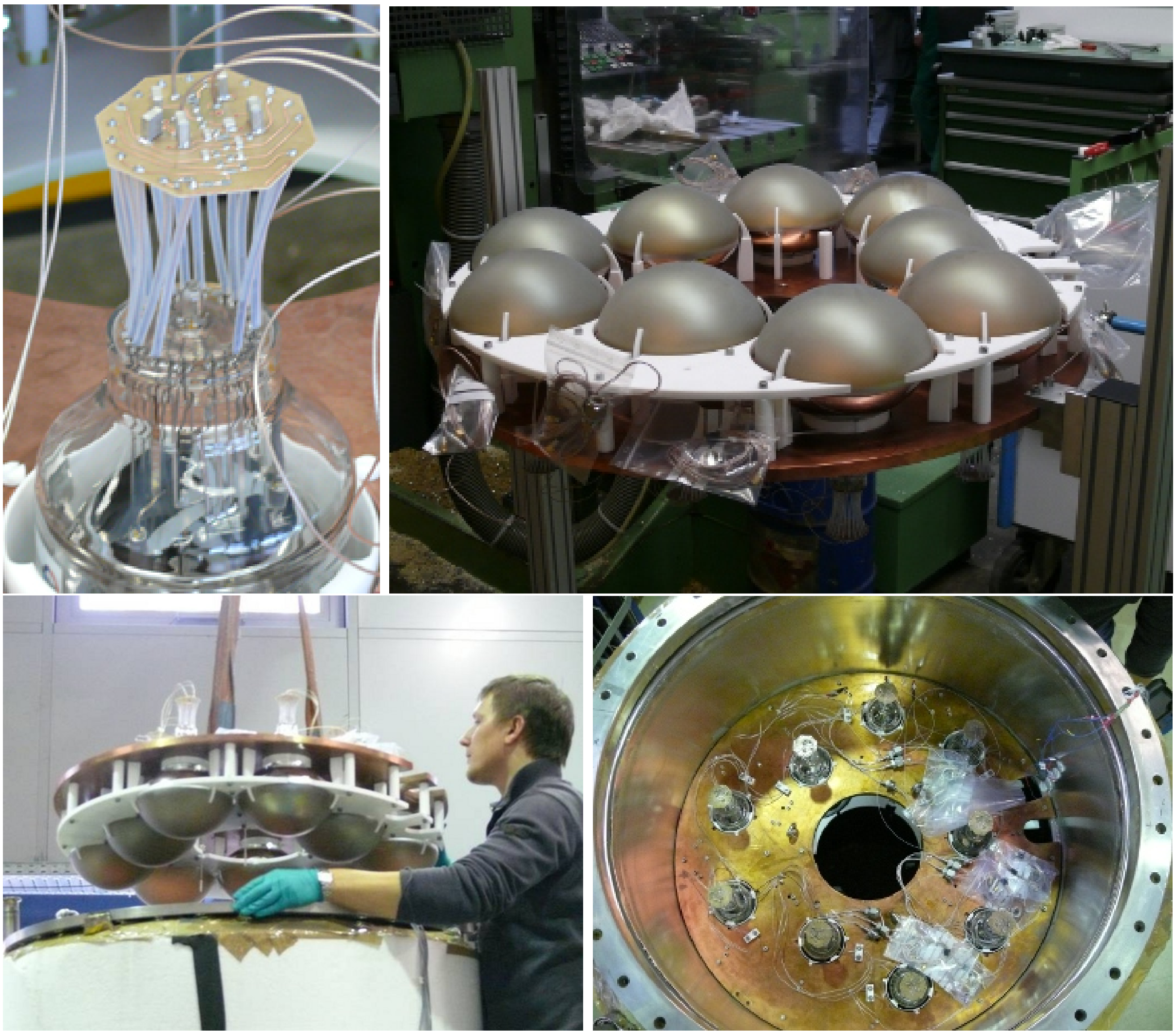

Figure 12: **Top left**: Photomultiplier with low-background voltage divider on a PTFE printed circuit board. **Top right**: Assembly of nine PMTs mounted in their low-background support. **Bottom left**: PMT assembly during test mounting into the cryostat. **Bottom right**: View into the cryostat with mounted PMT system.

7 Phase II detectors

The GERDA collaboration widened the scope of detector R&D for Phase II. In addition to segmented n-type detectors, thick-window p-type BEGe detectors with advanced pulse shape discrimination properties are considered for Phase II.

7.1 Prototype testing of segmented n-type detectors

Last year, we operated an n-type 18-fold segmented HPGe detector for five months in liquid nitrogen. Data with different radioactive sources were collected and are currently being analyzed. The background reduction was demonstrated to work with the simillar efficiency as with the detector in the vacuum cryostat.

After the detector was warmed up another cooling test was done to measure the electronic properties of the crystal. Capacity and leakage current were found to be in good agreement with the measurement done at Canberra.

Currently the electronic read out system is being modified to simulate better the conditions in the final experiment. The first amplifier stage (FET transistor) is separated from the preamplifier board and is moved in the liquid nitrogen. Operating electronics directly in liquid nitrogen poses some difficulties but the first tests with the new setup are promissing and show an improved stability over the old design.

In addition a 19-fold segmented prototype is operated in a vacuum cryostat. The detector is identical with the 18-fold segmented prototype (6-fold segmented in the azimuthal angle and 3 fold along the vertical axis) except for the 19th segment which is a 5 mm thick circular segment on top of the detector. The 19th segment is used to study surface effects. The top surface was scanned with an ^{152}Eu source, which has a low energy 121 keV gamma line. The test was finished and currently the data are being analyzed.

7.2 Crystal pulling R&D for Phase II

After two purification tests done at PPM Pure Metals (reported in previous Progress Reports), the yield and the purity of the material were satisfactory. Nevertheless we decided to process the remaining amount of depleted germanium with the secondary goal of providing enough 6N material to IKZ for crystal pulling tests.

From the original 50 kg GeO_2 we still had 26.7 kg which we handed over to PPM to repeat the same procedure as during the second test: reduction followed by three successive steps of zone-refinement. There were no losses during the reduction (yield = 99.3 %) and the zone-refinement yield was 83.9% with 15.5 kg 6N metal produced.

PPM was asked to recycle the remaining material from previous tests and zone-refine it again. As final result, from 49.2 kg of GeO_2 handed over to PPM, 30.2 kg 6N germanium metal was produced which coresponds to 88% total yield. It is worth to mention that without a reduction that went wrong, because of a simple mistake, the yield would be above 90%. Almost all the 6N material was shipped to IKZ and it was already used in many crystal pulling tests.

Until now IKZ produced ten Czochralski crystals in total and we can say that the crystal pulling, from the mechanical point of view, is under control. Unfortunately it was found that the Czochralski puller is the main source of impurities (As) and continuous upgrades are being made to achieve detector grade purity. During the last two experiments an impurity level of (10^{11} - 10^{12}) cm^{-3} net donor concentration was achieved which is an order of magnitude better than previous results. Presently the Czochralski puller is being modified to further reduce the impurity level.

To assess the purity of the 6N germanium produced at PPM, IKZ grew two float-zone crystals directly from the zone-refined ingots. The purity of these crystals was surprisingly good, (10^{10} - 10^{11}) cm^{-3} close to the seed end, in one case even reaching detector grade purity. This makes us confident that detector grade crystals can be grown directly from the PPM material without additional purification.

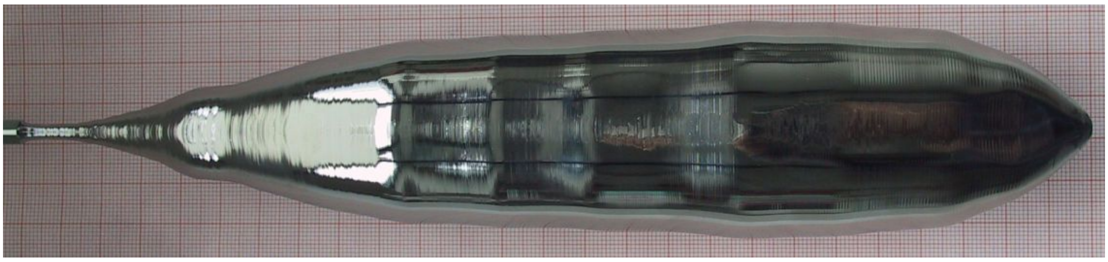

Figure 13: Czochralski crystal number 9. The donor concentration of this crystal is around $6 \times 10^{11}/cm^3$

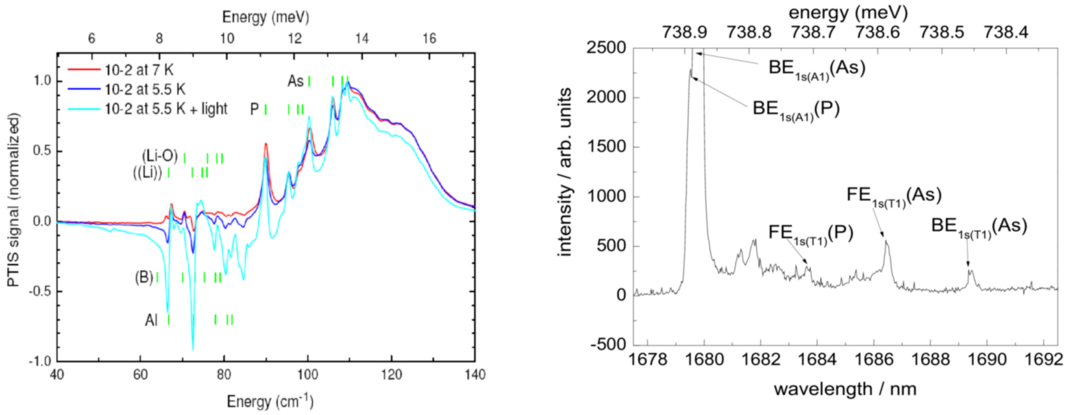

Figure 14: Comparison of PTIS (left) and PL (right) spectra of the same crystal

7.3 Crystal characterization

All the crystals produced so far were sampled and analyzed with low temperature Hall-effect measurements and Photo-Thermal Ionization Spectroscopy (PTIS).

Additional crystal characterization is carried out by the TU Dresden group using Photo-Luminescence spectroscopy (PL). To validate the method they used samples already characterized at IKZ. The bound-exciton lines seen in the PL spectra indicate the presence of the same donor impurities as the PTIS, namely phosphorus and arsenic (see Fig. 14). The two methods agree on the relative concentration of the impurities (line strength) and the distribution along the length of the crystal.

With PTIS and PL spectroscopy we have two independent methods to measure the chemical composition of the impurities.

7.4 BEGe detector R&D for Phase-II

The research and development with thick-window BEGe p-type detectors, candidate detectors for Phase-II, was further pursued during the period under report. The experiments were carried out with a 0.8 kg thick-window BEGe detector from Canberra Semiconductor NV, Olen, operated in a vacuum cryostat and details can be found in [3]. External ^{60}Co gamma radiation survives the pules shape discrimination cuts at $Q_{\beta\beta} = 2039$ keV with a probability of (0.93 ± 0.08) %, ^{226}Ra gamma radiation with (21 ± 3) %, and ^{228}Th gamma radiation with (40 ± 2) %. This background suppression is achieved adjusting the acceptance of the ^{228}Th double escape events (DEP), which are similar in topology to double beta decay, at (89 ± 1)%. The survival of different backgrounds together with the acceptance of the double escape peak are displayed in figure 15.

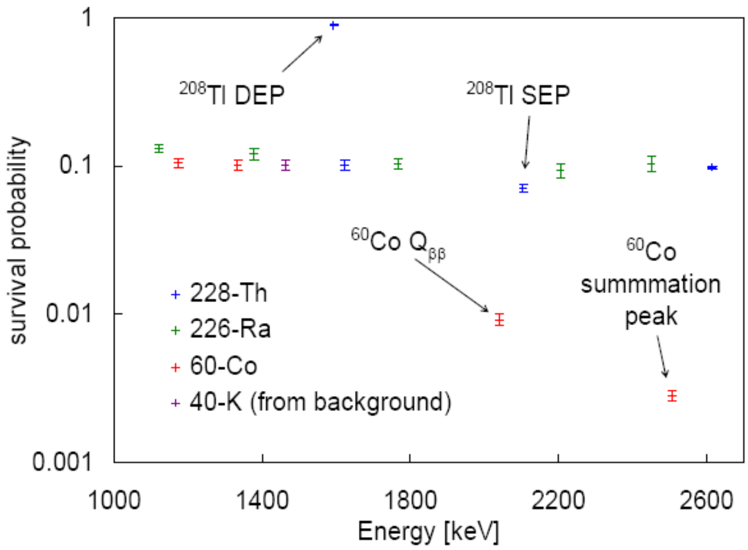

Figure 15: Survival probabilities of spectral peaks from different sources after pulse shape cut. The peaks that are not full energy peaks (FEP), as single (SEP) or double escape peaks (DEP), and summation peaks, are highlighted. Plotted in addition to peaks is the survival probability of ^{60}Co events near the energy of ^{76}Ge $Q_{\beta\beta}$.

Double escape events occur with a higher probability at the edges of the crystal, while double beta decays are homogeneously distributed. Tests were performed to check for a possible position dependence, and, apart from interactions close to the signal contact, no position dependence of the pulse shape discrimination has been observed. A further point of study concerned the energy dependence of the pulse shape cut. It could be shown that the cut derived from the DEP and from Compton scattering without coincidence tagging can be reliably applied at $Q_{\beta\beta}$ energies. The final point of investigation concerned the long term stability measured over a period of two months under continuous gamma irradiation which showed that the pulse height spectra and the charge collection are stable in time.

Based on the encouraging results, the collaboration decided to investigate further in depth the feasibility and production yield of thick-window BEGe type detectors from enriched germanium material for Phase-II. For this purpose, a full production test with depleted germanium has started in January 2009. Additional 34 kg of depleted germanium oxide has been ordered from ECP and will be delivered by the beginning of May. The material will be subsequently reduced and purified at PPM Pure Metals and shipped to Canberra-US for crystal pulling. From this material, several thick-window BEGe detectors will be produced for testing and for the evaluation of the expected production yield from enriched germanium material.

8 Calibration system

To concentrate the activities related to the Gerda calibration system, a new task group (TG-12) was formed in February 2009. Some of the immediate responsibilities are Monte Carlo simulations of the required source types, strengths and collimators, of the induced gamma and neutron backgrounds, as well as the fabrication and test of custom-made, low-neutron emission sources and collimators. Near-future responsibilities are the long-term maintenance of the calibration system and stability monitoring of calibration parameters.

8.1 Monte Carlo simulations of source strengths and positions

Using the MaGe framework, we scrutinized different types of radioactive sources, under the following requirements: reasonable half lives ($T_{1/2}$ >1 year), full energy peaks over the entire range of interest (∼0-3 MeV), a peak close to the Q-value of 2039 keV, a double-escape peak yielding a population of single-site events for pulse shape calibration, sufficient statistics in the main peaks to be used in the calibrations (peak-to-background ratio $\geq$ 3:1 in the 3σ region around the peak). Taking these aspects into account, we decided to use ^{228}Th, with $T_{1/2}$=1.9 yr. The Monte Carlo spectrum in one of the Ge crystals is shown in figure 16.

In the subsequent step we determined the minimum strengths, as well as the optimal z-positions of the calibration sources. We have used the phase I configuration of detectors with the final lock and planned x-y positions for the three calibration sources. The collimator will be described in Section 8.2. With 3×10^9 simulated ^{228}Th decays per position,

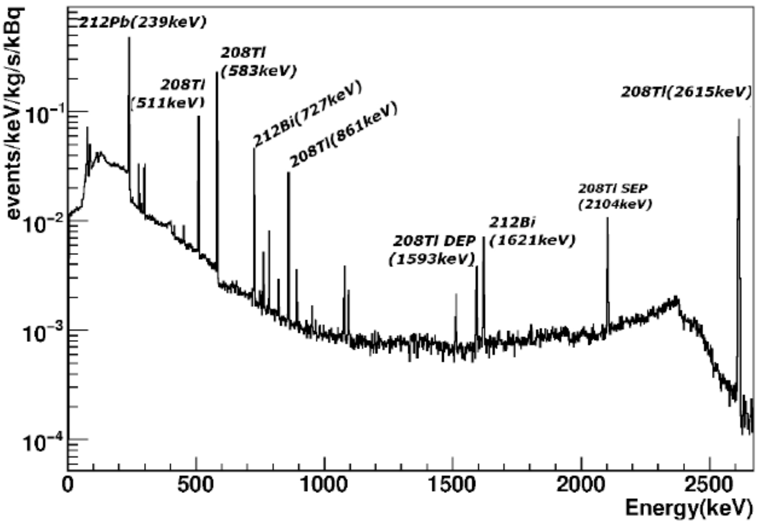

Figure 16: Monte Carlo simulation of a ^{228}Th calibration spectrum in one Gerda HPGe crystal.

we systematically scanned the z-direction, determining an activity of 20 kBq/source (for 25 min calibration time per layer) and following optimal positions for each of the three detector layers: $z_1 = -70$ mm, $z_2 = -210$ mm and $z_3 = -370$ mm ($z = 0$ being the top edge of the first detector layer). Considerations relevant for above study were a compromise between high event rates in calibration mode versus low-backgrounds in parking mode, and the statistics in the ^{208}Tl single escape peak (which is with E=2104 keV closest to the Q-value of the ^{76}Ge double beta decay) in each detector. One problem, which can not be solved by increasing the activity of the source, is the statistics in the double escape peak at 1593 keV, with a rather poor peak-to-background ratio of ~1:2 (1:3) in the 3σ (2σ) region around the peak. We are investigating possibilities of reducing the Compton-background in this region. This work will be repeated with the preliminary lock geometry.

8.2 Absorber, source production and backgrounds

Since the sources will be parked inside the LAr cryostat, a proper shielding by the source collimator is required. It should be made of a radiopure material with high absorption and good mechanical properties. We have considered three different materials: tungsten (99.97), a W-alloy (Densimet, 92.5% W, the rest Fe and Ni) and tantalum. Their densities, as well as results of the screening with the Gator detector at LNGS are shown in table 1. Since Ta has the lowest activities (only upper limits were obtained for U/Th/K/Co/Cs) and pure W is hardest to machine, the material of choice is tantalum. The ^{182}Ta isotope, with $T_{1/2}$=114.4 d, has a Q-value of 1.8 MeV for the β^--decay (100%) and will not contribute to the background in the region of interest.

The preliminary design is a cylinder with a radius of 3.5 cm and a height of 6 cm, yielding a mass of ∼3.8 kg per absorber. We are currently studying the integration of the stainless steel source capsule (see below) into the absorber geometry. A full mock-up system will be tested in the liquid argon test facility at the University of Zurich, using a small n-type, HPGe detector immersed in LAr and its associated low-noise electronics.

Material	Tungsten	Densimet	Tantalum
Density [g/cm^3]	19.25	17.6	16.65
Activity [mBq/kg]			
^{238}U	300 ± 75	180 ± 30	< 11
^{232}Th	30 ± 10	70 ± 20	< 9
^{60}Co	< 8.1	7 ± 2	< 1.9
^{40}K	40 ± 20	< 57	< 33
^{137}Cs	< 6.0	< 5.1	< 2.5
^{182}Ta	–	–	52 ± 5

Table 1: Densities and material screening results for the three materials which have been considered as source collimators.

A problem with custom-made ^{228}Th sources is the neutron yield via (α,n) reactions in the porous ceramic pallet (NaAlSiO$_2$) containing the radioactive element. A calculation of the n-spectra and yields gave a total neutron production rate of about $4{\times}10^{-2}$ n/(s kBq) with a mean energy of 1.5 MeV. Subsequent neutron transport simulations in MaGe show that the background in the 1.5-2.5 MeV region is about $1{\times}10^{-3}$ events/(kg yr keV) for a total ^{228}Th activity of 100 kBq in parking position, which is already at the level of the Gerda phase II goal.

We have thus started a collaboration with PSI to fabricate sources embedded in gold, which has a 9.9 MeV threshold for (α,n) reactions, much higher than the light materials in ceramics and above the maximum α energy of the ^{228}Th chain. A 20 kBq ^{228}Th HCl-solution has been acquired and was processed at PSI at the end of March. In a series of chemical reactions the end product of ^{228}ThO$_2$ was obtained in a gold crucible, which was closed and mechanically rolled, before being sent for encapsulation in a stainless steel capsule and certification to Eckert&Ziegler, Berlin. Special care was taken to avoid foreign contamination in each of the involved steps. After the encapsulation, several wipe tests are planned, with the wipes being screened by the ultra-low background Gator detector at LNGS. We are also planning to measure the source itself with Gator and compare with the expected activity based on Monte Carlo simulations. If successful, the above procedure will be used for fabricating the actual Gerda sources.

Natural oxygen contains a fraction of 0.038% ^{17}O and 0.2% ^{18}O with threshold-energies of < 0.1 MeV and < 1 MeV for (α,n) reactions, respectively. Calculations of the neutron production rate in ThO$_2$ yielded $5 \cdot 10^{-4}$ n/(s kBq) with a mean neutron energy of 2.5 MeV (figure 17, left). This gives a mean neutron background which is two orders of magnitudes lower than for a commercial ^{228}Th source (figure 17, right). We are planning to directly measure this background with a ^{3}He neutron counter located underground at LNGS.

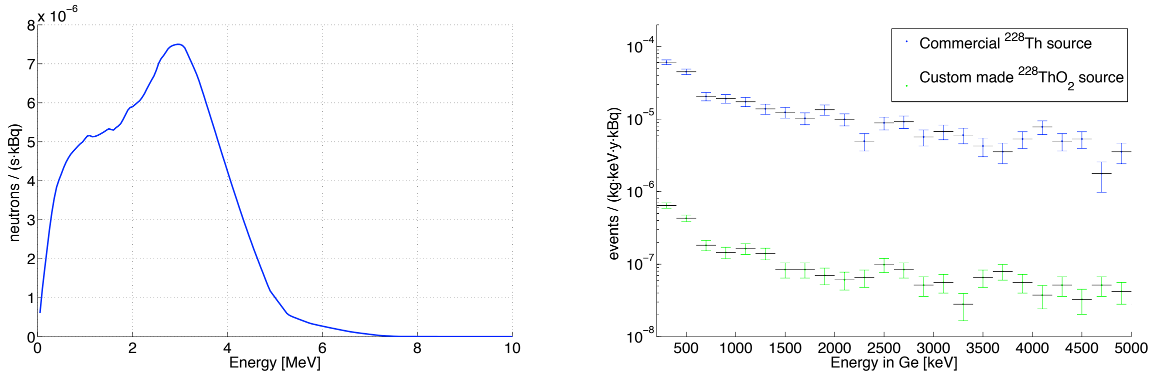

Figure 17: Left: Calculated neutron energy spectrum from the ThO_2 source; Right: Calculated energy spectra in the Ge detectors from neutrons emitted by commercial (blue) and custom-made (green) $^{228}ThO_2$ sources in the parking position, respectively.

The gamma backgrounds from the source and the collimator material in the parking positions have been estimated in a series of Monte Carlo simulations combined with analytical calculations of the shielding power of LAr. The mean free path of 3 MeV photons in LAr is about 21 cm. The resulting background from the Ta collimators is with $< 5.5 \times 10^{-9}$ events/(kg yr keV) negligible. For 3×20 kBq sources with a Ta absorber thickness of 6 cm, the background in the energy region of interest is $(1.9 \pm 0.4) \times 10^{-4}$events/(kg yr keV). To reduce this level by one order of magnitude, an additional 2 cm of absorber material is needed.

9 Status of Front End Electronics

9.1 The FE circuits

The Cuflon PCBs for the 3-channel circuits have been designed and 11 samples have been produced; 1 dummy, 4 for electronic and detector tests, 6 for the radioactivity screening. The ASIC circuit has been bonded on board and is mechanically protected by a Cu lid custom made. The tests have been performed both at the bench, with the SUB encapsulated detector, and with the naked detector. To minimize the number of cables and contacts in the pogo-pin matrix, all three channels in the PCB are powered through one cable for each low voltage power supply (V_{cc}, V_{ee}, V_{fet}). The protective diodes to prevent damage of the front end FET, as repeatedly happened in the tests of the single channel circuit in summer 2008 when connecting/disconnecting the detectors, have been included. Figure 18 shows the PCBs with the SMD component finally mounted.

The table shown in Fig. 18 reports the relevant features of the PZ0 circuit as measured at the test bench with short cables and at room temperature: the circuit shows good spectroscopic performance and adequate bandwidth to perform pulse shape analysis with germanium diode detectors. A capacitive cross-talk among the 3 channels has been measured at a level of 1.5%-2%; it is deterministic and can be corrected via a cross talk matrix.

9.2 Results coupling FE to detector and FADC readout system

In the measurements with the encapsulated detector the FE circuit is located in liquid nitrogen near the detector and is connected to the FADC or spectroscopy amplifier either with 2 m long cables or with 12 m long cable (RG178, Resistivity 0.8 Ω/m). As shown in Fig. 19, with 2m long cables a resolution of 2.6 keV at the 1.275 keV ^{22}Na line has been measured both by analog (through the analog gaussian filter at $\tau_{shaping}$=10 μs of the spectroscopy amplifier) and digital processing. In the digital processing, the signals from the cold preamplifier circuit are acquired by means of the 14 bit, 100 MHz, FADC. The algorithm applied to define the energy is the Jordanoff (trapezoid) one. The attained resolution allows to well resolve the ^{228}Ac at 1588.92 keV from the ^{228}Tl double escape peak line at 1592.53 keV, when the detector is irradiated by a ^{232}Th source. In the same energy region the ^{212}Bi 1620.5 keV and ^{228}Ac 1630.62 lines are visible and well resolved.

The resolution attained at the pulser line (1 MeV injected) is 2.0 keV for the channel with the detector connected, and 1.6 keV for the two other channels (no detector connected in these tests). When the cold circuit is connected to the processing electronics through a 12 m long RG178 cable, the resolution worsens a bit: 2.6 keV for analog processing and 2.8 for digital processing.
In a short test with the 3-channel circuit coupled to the naked detector in the underground laboratory, a resolution of 3.5 keV at the 1332 keV ^{60}Co line has been obtained; the same value was achieved in the summer 2008 measurement campaign with the 1-ch circuit. The origin of the parallel excess noise responsible of the resolution degradation when coupling

the cold circuit to the naked detector needs further experimental investigations.
A significant crosstalk (8%) among the three channels through the common low voltage power supplies has been observed when operating with the long cables and the detector, therefore more tests at the bench are currently ongoing to eliminate this effect, optimize the bandwidth and the dynamic range. Another option is to provide independent power supplies to the three channels.

Six PCBs with all the SMD components mounted have been screened to evaluate their radioactivity. The overall ^{232}Th content is 220 μBq per PCB that is well below the 500 μBq limit required to keep the background index in the detectors below 1 x 10^{-3}, while the ^{226}Ra content is extremely high (6.5 mBq/PCB). The responsible components have been found to be the capacitors of type X5R and X7R used to filter on board the low voltage power supplies. Some options to reduce the number and the size and eventually change the capacitor type are under investigation.

Finally, a simple Cu support and EM shield for the PCB, PTFE guides for the detector to FE cables, PTFE clamps for the HV and signal pins to be located at the top of the GERDA string have been designed, produced and delivered for first tests with mockups. These pieces will be used and tested in the spring integration tests at the LNGS Hall di Montaggio where the circuit will be tested for the first time with three detectors connected to the inputs.

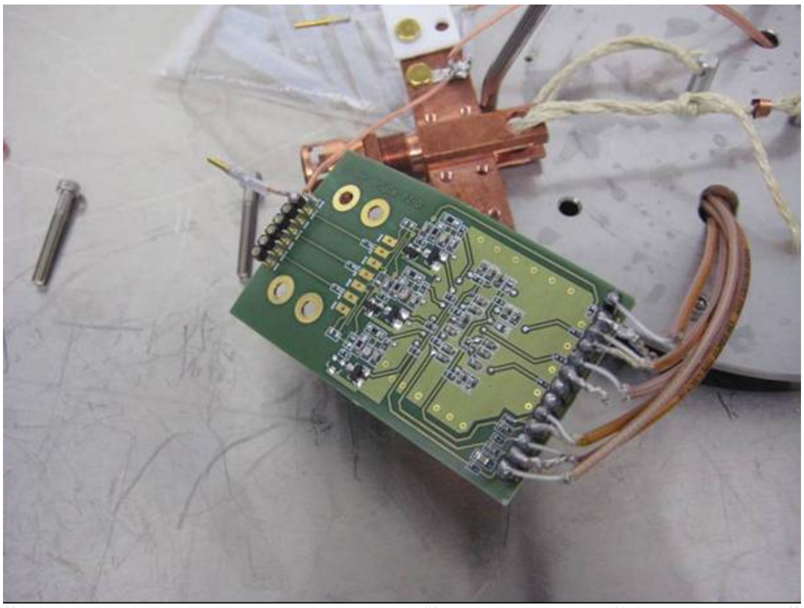

$C_F = 0.2$ pF, $C_{det} = 33$ pF	Channel 1	Channel 2
Gain - 1 MΩ term.	258 mV/MeV	284 mV/MeV
Gain - 50 Ω term.	134 mV/MeV	148 mV/MeV
Gain - 150 Ω term.	197 mV/MeV	218 mV/MeV
Output voltage swing - 1 MΩ term.	2.745 V	2.770 V
Input energy dynamic range	10.64 MeV	9.75 MeV
ADC energy range (1V) - 1 MΩ term.	3.87 MeV	3.52 MeV
ADC energy range (1V) - 50 Ω term.	7.46 MeV	6.76 MeV
ADC energy range (1V) - 150 Ω term.	5.08 MeV	4.59 MeV
Rise time - 1 MΩ term.	26.4 ns	27.9 ns
Rise time - 50 Ω term.	35.8 ns	38.3 ns
Rise time - 150 Ω term.	31.2 ns	33.6 ns
Fall time	172 μs	175 μs
ENC ($\tau = 6$ μs)	158 e^-	151 e^-
FWHM ($\tau = 6$ μs)	1.083 keV	1.041 keV

Figure 18: Top: The 3-channel PCB; the three FETs are visible. The ASIC circuit protected by a Cu lid is on the bottom side. Bottom: A table listing the relevant features as measured at the test bench at room temperature.

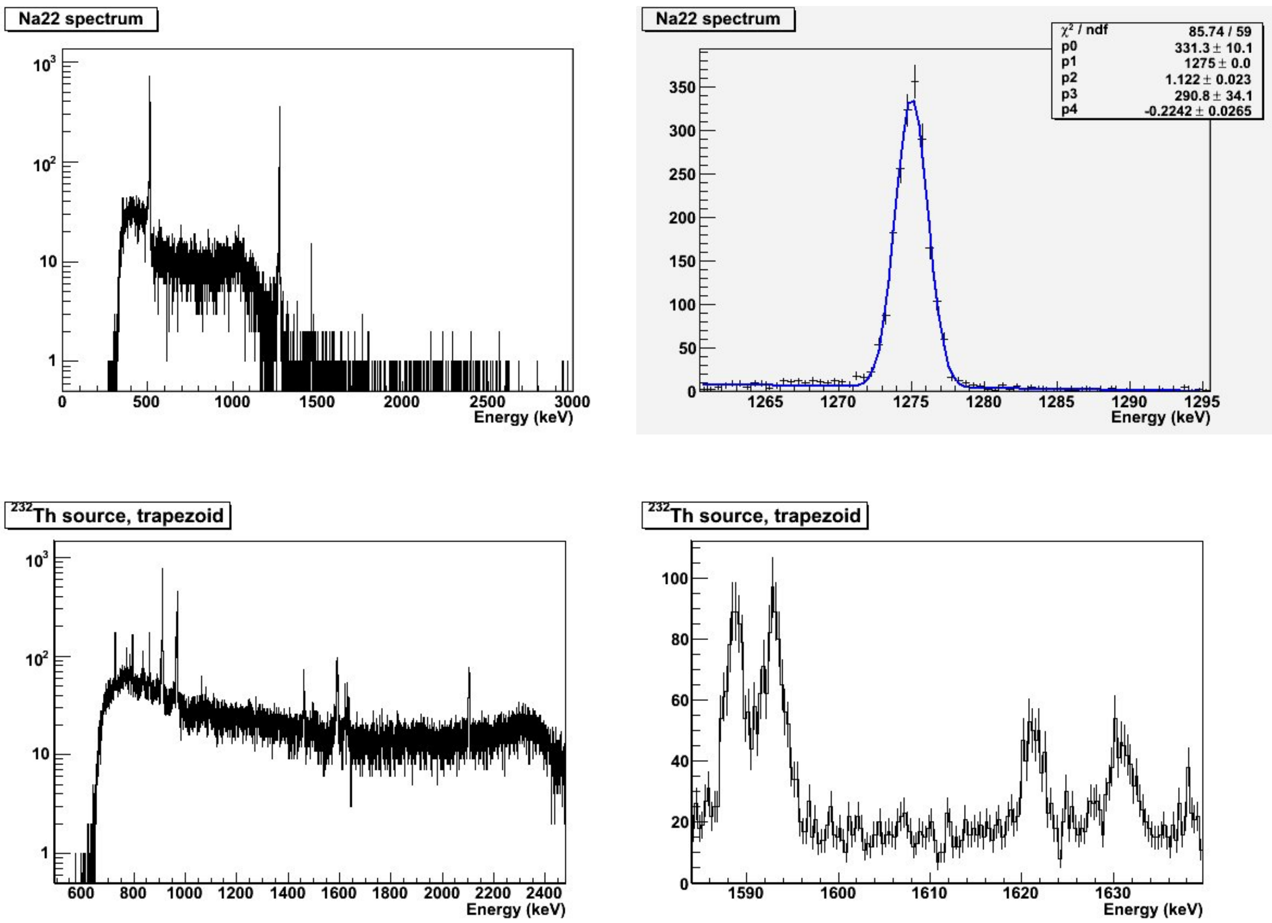

Figure 19: ^{22}Na (top) and ^{232}Th spectra acquired with a 100 MHz 14 bit FADC using the trapezoid Jordanoff algorithm. The resolution is found to be 2.6 keV FWHM at the 1275 keV line.

10 DAQ electronics and online software

In this section it will be illustrated the progresses made in the definition of the network structure and, at the end, the planned activities for the phase II electronics.

10.1 GERDA network structure

In these last months, the activities were completely dedicated to the definition and setting-up of the network structure for the GERDA building in Hall A. The network of the underground laboratories is connected to the external labs by means of a certain number of optical fibers which are shared among the different experiments according to their throughput needs. Two multimodal optical fibers have been explicitly dedicated to the GERDA experiment. The path of the GERDA optical fibers ends outside the experiment building, where in a small cabinet, the fibers are connected to a network switch [5]; the latter provides 44 auto sensing ports (10/100/1000) and offers access security and advanced prioritization and traffic-monitoring capabilities. The different network lines are routed inside the GERDA rucksack.

The switch is directly connected to a dedicated server [6] which provides network routing facilities and acts as a firewall and user authentication server. At the moment, this is the only public service available directly from the external networks and should be used to access all GERDA internal network resources and services. The server has two network interfaces, one connected to the LNGS public network and a second port connected to the `GERDA` virtual LAN. A Port Address Translation (PAT) network device will be used, internally, to translate TCP/UDP communications between GERDA private network computers and public network hosts.

Figure 20 shows the layout of the GERDA local network. Two separate logical networks are visible: the DAQ/Slow Control network, where mission critical machines are connected, and a network branch for user laptops and computers temporarily connected to the LAN.

10.2 Network services

The following centralized services are available:

`NIS` server for user authentication;

`DNS` server for host name resolution;

`DHCP` server for the DAQ/Slow Control machines and all the computers attached temporarily to the network (i.e. laptops);

`Web` server for the whole experiment.

Additional resources, provided by the individual groups of the GERDA Collaboration, will be made available on demand. Their availability will be achieved through the PAT network device. As an example, it will be possible to access the Web Servers of specific

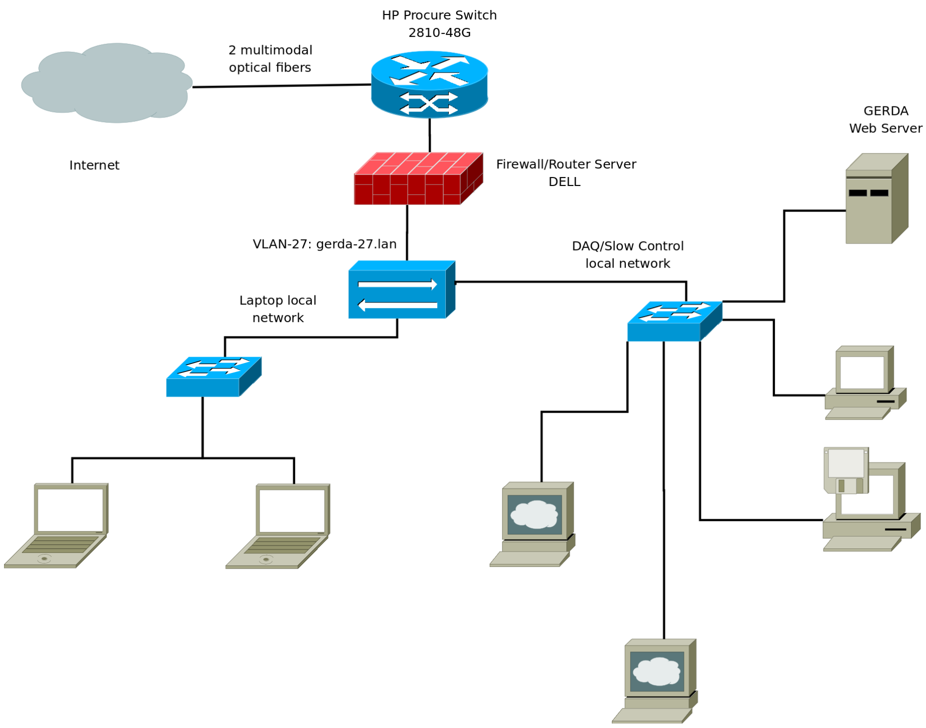

Figure 20: GERDA Network layout. A description of the different parts is given in the text.

components from the outside network, only by authorized experts, for hardware monitoring and parameter setting purposes.

10.3 Access to the GERDA network resources

As stated previously, the GERDA network access point is provided by the server, this is the only computer available for direct access from the outside network.

In order to provide access to internal GERDA resources (mainly internal Web servers), a `proxy` service has been setup. Once configured, it will be possible to access internal Web servers, through the main GERDA Web server.

As an example, we need access to the local web server provided by the Alarm Dispatcher Unit. The local web server is running on the port 80, but the machine is not visible from the outside network. Using the `proxy` server, the Alarm Dispatcher Web server can be reached through the GERDA Web server, at an appropriate URL.

10.4 Phase II electronics

The data acquisition for the phase II germanium detector readout is based on Struck SIS3301 flash ADCs. The FADCs and the trigger controller for this system are available. In the next months, VME based fanout modules for the clock distribution will be acquired and the firmware for the trigger controller will be developed. This controller is identical to the one which will be used for the muon detector readout since the latter is using the same FADCs for readout.

11 Simulations and background studies

11.1 Simulation of the GERDA background spectrum

The MCC2 (Monte Carlo Campaign 2) campaign is one of the major ongoing activities of the GERDA Task Group 10, which is devoted to Monte Carlo simulations and background studies. The MCC2 campaign aims at the production of a realistic energy spectrum of the GERDA experiment (also in the energy region below $Q_{\beta\beta}$), as previously discussed in [7]. In the experiment, many elementary types of physics events will contribute to the total energy spectrum, e.g. radioactive contaminations in various parts of the experimental structure, cosmic-ray muons directly deposing energy in the germanium crystals or producing radioactive isotopes in the experimental set-up, etc. Using the GEANT4-based MAGE framework [8], which is jointly developed by the GERDA and MAJORANA Monte Carlo groups, one energy spectrum for each elementary contribution is simulated. To get the final expected spectrum in GERDA, first one needs to rescale the elementary spectra with respect to a set of physics parameters (e.g. specific activities, half-lives, etc.), and then to add them up. Due to the large number of contributions one has to deal with a large number of parameters and elementary spectra. To solve this task in a clear and maintainable way, a dedicated framework is under development, whose basic design idea is to have one single set of input parameters and one single set of contributions. This ensures self-consistency and easy editing and modeling of the total spectrum. Figure 21 shows an example spectrum produced by the framework taking into account double beta decay in the detectors and radioactivity in the crystal holder.

11.2 Dedicated Monte Carlo simulations

Other individual background sources have been considered in more detail, also in connection with the activity of other task groups, to settle specific issues or to validate MAGE-based simulations.

11.2.1 Background from external γ-rays

Background due to external γ-rays (either from the cryostat or from the laboratory walls) has been re-evaluated using a dedicated fast simulation code (not based on GEANT4 or MAGE) developed by INR-Moscow. Results can be used to cross-check and validate MAGE-based simulations, having been obtained with a completely independent approach. The background at $Q_{\beta\beta}$ from the 2.6-MeV γ-ray from ^{208}Tl is about $1.2 \cdot 10^{-5}$ cts/(keV·kg·y) and $8 \cdot 10^{-6}$ cts/(keV·kg·y) for the stainless steel cryostat (including the inner Cu layer) and for the laboratory rock, respectively [10]. From the background

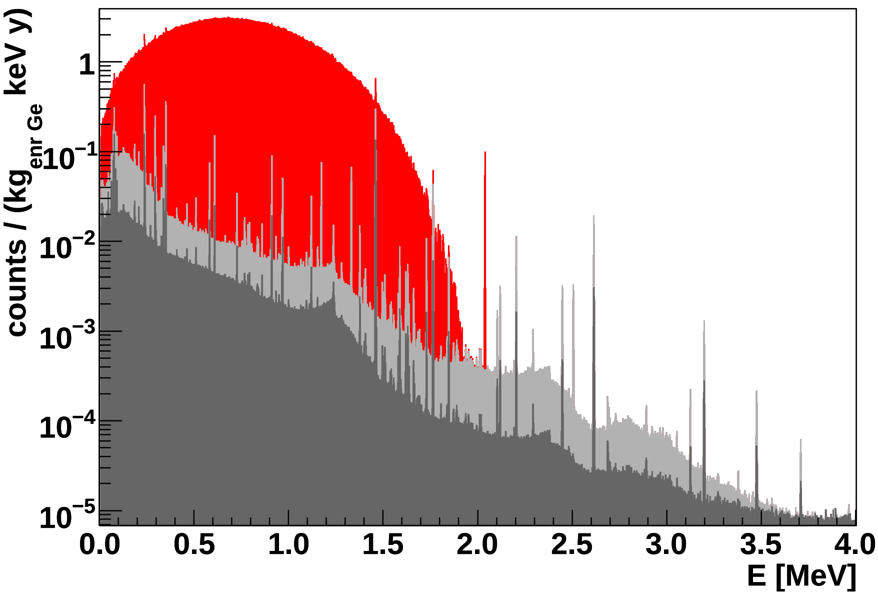

Figure 21: Energy spectrum assembled by the contributions from 0ν- and 2ν- double beta decay in the crystals (red) and radioactive contaminations in the crystal holders. Half-lives for double beta decay are assumed to be $T_{1/2}(2\nu) = 1.74 \cdot 10^{21}$ y [9] and $T_{1/2}(0\nu) = 1.2 \cdot 10^{25}$ y, after Klapdor-Kleingrothaus *et al.* [9], respectively. For some contamination levels only upper limits are known (bright grey), for others central values were measured (dark grey).

estimates presented above it is clear that the GERDA background is expected to be largely dominated by internal sources (radioactivity in the crystals and in the close parts).

11.2.2 Background due to ^{222}Rn emanation from the cryostat

Dedicated MAGE-based simulations were run to evaluate the impact of the ^{222}Rn emanation from the cryostat, which was measured to be about 30 mBq. Previous simulations were run with the assumption that the activity of ^{222}Rn and daughters (specifically, ^{214}Bi) is uniformly distributed in the full liquid argon (LAr) volume. With this assumption, the background index at $Q_{\beta\beta}$ turns out to be about $4 \cdot 10^{-4}$ cts/(keV·kg·y) for the Phase I array[1], which is reduced only by 15% using the anti-coincidence cut. A result of the same order is obtained also for the Phase II array[2].
It has been realized that the assumption of uniform radon distribution in LAr is too optimistic, since convection is expected to transport radon from the cryostat walls to the vicinity of the crystal array. Dedicated simulations were re-run considering more real-

[1]Eight ^{enr}Ge detectors from Heidelberg-Moscow and IGEX plus 6 ^{nat}Ge detectors from GTF, that are used only for anti-coincidence.

[2]Same crystals as for Phase I plus 14 n-type 18-fold segmented ^{enr}Ge detectors.

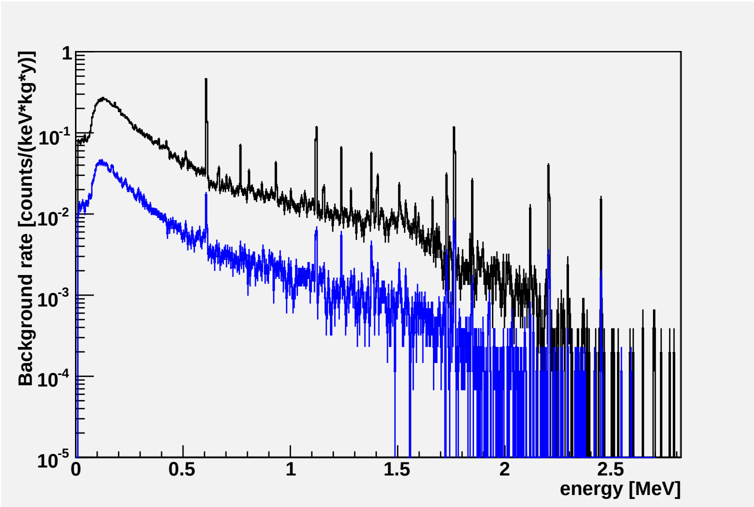

Figure 22: Background spectrum in the GERDA Phase I set-up due to 30 mBq of ^{214}Bi (from the ^{222}Rn chain) in LAr. Decays are not distributed uniformly in LAr, but on convection layers located on the walls of the cryostat (10 cm thick) and in the center of the cryostat (60 cm radius), where the detector array is deployed. Black and blue spectra refer to the conditions without and with the proposed anti-Radon shroud, respectively.

istic assumptions for the radon distribution in LAr, resulting in a background rate of $2 \cdot 10^{-3}$ cts/(keV·kg·y) (Phase I array, no cuts) for 30 mBq emanation rate. In order to mitigate the effect of ^{222}Rn emanation from the cryostat, it was proposed to build a thin cylindrical shroud around the crystal array, starting from the cryostat neck. This would prevent to have ^{222}Rn at small distance ($<$ 40 cm) from the detectors. Simulations show that in this case the background produced by 30 mBq of ^{222}Rn is about $1.5 \cdot 10^{-4}$ cts/(keV·kg·y) (Phase I array, no cuts), which is acceptable for GERDA. Figure 22 shows the Rn background spectrum in the GERDA Phase I set-up assuming a realistic convection-driven Radon distribution in the liquid argon volume without (black) and with (blue) the shroud. The background contribution from the shroud itself because of its ^{232}Th contamination is estimated to be $< 0.2 \cdot 10^{-4}$ cts/(keV·kg·y), for a 50 μm-thick Cu shroud having $< 20\mu$Bq/kg in ^{232}Th.

11.2.3 Efficiency of the Cherenkov muon veto

A final Monte Carlo study was performed for the muon veto to evaluate the effect of different trigger conditions on the expected efficiency. The simulation is carried on with MAGE and it explicitly accounts for the Cherenkov light produced by muons and muon-induced showers.
The simulated set-up includes 66 photo-multipliers, that are grouped in 10 FADC boards. Table 2 summarizes the results. A suitable trigger condition is a four-fold FADC majority

within 30 ns. In this case, the identification efficiency for muon-induced events that produce an energy deposit in the detector array is 99.56%; the rate of accidentals is $< 5\%$ with respect to physical μ events in the Cherenkov veto (2.2 muons per minute).

Table 2: Expected efficiency for different trigger conditions. In total 56,252 muons with energy deposition in the crystals, corresponding to 14 years of data taking, were simulated.

# FADCs majority (30 ns)	muons detected	expected efficiency [%]
3	56163	99.84
4	56005	99.56
5	55545	98.74
6	53861	95.75
7	39186	69.66

11.3 Simulation of pulse shapes from Ge detectors

In the last months significant progress toward a realistic pulse shape simulation of a true coaxial 18-fold segmented Phase II prototype detector has been made. The calculation of the electric field inside the germanium detectors was improved. Now any impurity density profile can be simulated. The calculation of the weighting potentials was improved by including a more realistic treatment of the segment boundaries.
A first comparison between data and simulation has been made. Charge pulses were taken with a ^{152}Eu source placed in different positions. To compare with the simulated pulse shapes, the full pulse shape simulation chain was used. A beam of 121 keV photons was simulated using MaGe. The resulting distribution of energy deposits inside the detector was used to simulate pulse shapes accordingly. About 500 pulses were taken in each source position. They were averaged into one pulse, in which the noise is canceled out while the main shape remains. The simulated pulses were treated in a similar way, and the averaged simulated pulse was compared to the averaged pulse from data. This is shown in Fig. 23. The agreement is in general very good. The residual difference in shape might be explained by incomplete modeling of the electronic properties of the front-end electronics as well as by a not fully realistic impurity density profile.
Further effort will be put into the measurement of the impurity profile, in order to adapt the simulation accordingly. An improvement of the electronics model is aimed for and an estimate of the systematic uncertainty of the simulation is planned.

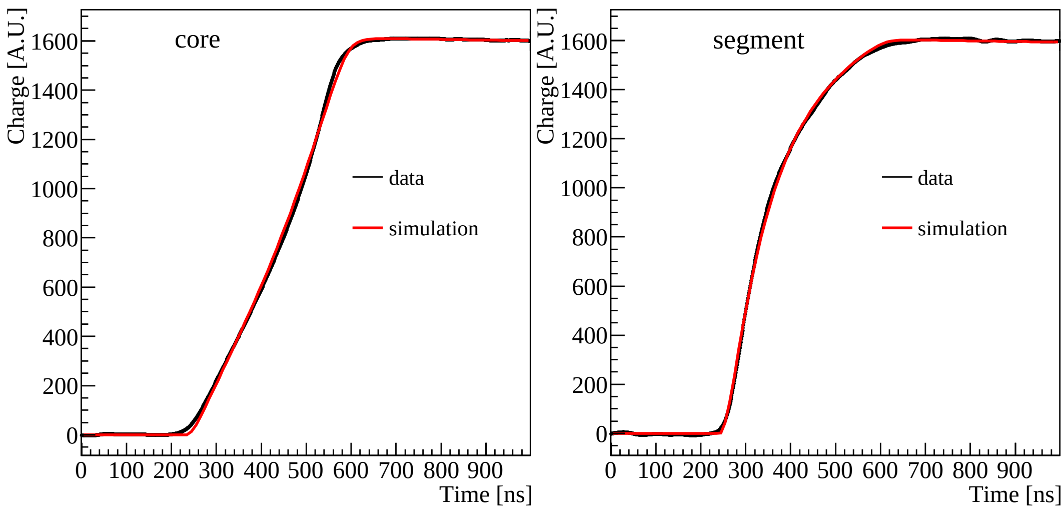

Figure 23: Comparison between simulated and recorded pulses for the core and the segment. All recorded and simulated pulses have been averaged resulting in a single pulse each.

12 Material screening

12.1 Radon emanation measurements

Several samples have been investigated in terms of ^{222}Rn emanation. The obtained saturation results are collected in Table 3. Uncertainties are given at 1 σ and upper limits at 90% confidence level. TIG welds done applying 62 A current in argon atmosphere produced less than 0.03 mBq/m after only rough cleaning (brushing, acetone washing). As a reference sample steel plates of the same surface without welds were tested (row 1 of Table 3). A plastics for sealing (Delrin) and a CF-40 flange with a glass window to be installed in the cryostat produced lower than 50 μBq and 20 μBq, respectively. A displacement measuring device, to be used in the cryostat as well, showed a higher value of 0.36 mBq, which is however still acceptable. Steel encapsulated PT100 temperature sensors gave only about 7 μBq/piece. The highest emanation rate of about 1 mBq has been detected for the big shutter valve. It was tested in the "open" state by closing its both sides with metal sealed flanges. The LAr supply line from valve box to cryostat which is part of a three-axial LN_2/LAr supply line emanates 0.25 mBq.

Sample	Emanation rate	Remarks
Steel plates without welds	< 0.1 mBq < 0.4 mBq/m^2	4 plates, 0.26 m^2 (brushed, acetone wiping)
Steel plates with TIG welds	< 0.1 mBq < 0.03 mBq/m	4 plates, 3.2 m, 62 A (brushed, acetone wiping)
Delrin	< 50 μBq	Cylinder, 380 cm^2, 43 g
PT100 sensors	(6.6 ± 0.5) μBq/piece	Steel encapsulated
Displacement measuring device	(0.36 ± 0.03) mBq	To be installed in the cryostat
CF-40 flange with a glass window	< 20 μBq	To be installed in the cryostat
Shutter valve	(0.92 ± 0.03) mBq	To be installed in the cryostat
Three-axial cryo-line (for LN_2/LAr)	(0.25 ± 0.04) mBq	Cryogenic infrastructure

Table 3: ^{222}Rn emanation from different samples.

A ^{222}Rn emanation measurement of the cryostat after additional cleaning has been performed (with improved accuracy) in November 2008. In addition we have checked whether or not the radon was homogeneously distributed in its big volume by taking samples from the bottom and from the top. The result was positive (Rn homogeneity) and the total emanation was found to be 30.6 mBq, showing very minor cleaning impact. The results of all the cryostat emanation tests are summarized in Table 4.

Sample description	Single results [mBq]	Average [mBq]	Comments
1^{st} test, SIMIC November 2007	$16.9 \pm 1.6_{stat} \pm 3.0_{sys}$ $29.8 \pm 2.4_{stat} \pm 5.8_{sys}$	23.3 ± 3.6	Empty cryostat after cleaning
2^{nd} test, SIMIC/GS March 2008	$13.6 \pm 0.7_{stat} \pm 2.4_{sys}$ $13.7 \pm 0.7_{stat} \pm 2.7_{sys}$	13.7 ± 1.9	Empty cryostat, after additional cleaning performed at SIMIC
3^{rd} test, GS June 2008	$33.0 \pm 2.8_{stat} \pm 7.0_{sys}$ $35.7 \pm 2.9_{stat} \pm 8.8_{sys}$	34.4 ± 6.0	After copper shield mounting
4^{rd} test, GS November 2008	$33.2 \pm 3.5_{stat} \pm 1.9_{sys}$ $31.3 \pm 4.6_{stat} \pm 3.4_{sys}$ $27.3 \pm 2.4_{stat} \pm 0.7_{sys}$	30.6 ± 2.4	After wiping of Cu / steel surface Precise pressure reading.

Table 4: ^{222}Rn emanation from the GERDA cryostat at different preparation stages.

12.2 Radon monitoring

The long-term measurements with the electrostatic radon monitor which were mentioned in the last progress report worked well without problems. For nitrogen, 40 kV was used with a collection efficiency of 76% for ^{218}Po. For argon an efficience of 95% was achieved with 8 kV. With 12 kV, there was no efficient improvement in collection detectable.

The radon emanation of the 711 liter vessel including all pipes was determinated to be ~ 1 mBq. Using a steady gas flow through the radon monitor of 6 l/min, the gas will be replaced every 2 hours. In this condition and if the monitor is not operated in loop mode the background due to radon emanation will add about 15 μBq to the signal. For a flow rate of 3 l/h it will add about 30 μBq. Since the background contribution is known it can be subtracted afterwards.

The two-amplifier technique allowes to use an in-sito pulse shape analysis to discriminate noise. Therefore, the positive and negative signals of the Si-PIN diode are measured. The resulting background varies depending on the peak energy between 0.2 and 2 counts per day. By using the definition of a detection limit by a signal to noise ratio of 1, a limit between 7 μBq and 70 μBq can be achieved.

Spare electronics and Si-PIN diode detectors are built up to have a fast replacement possibility. Within the next month, the electronics rack will be installed and tested. The transport of the radon monitor to LNGS is planned in May 2009.

12.3 Behaviour of radon in liquid nitrogen

The recently mentioned plan of measurements (LNGS-EXP 33/05 add. 7/08, Appendix, par. 11.3) was accomplished. We were investigating the behaviour of radon dissolved in liquid nitrogen.

We have performed measurements using a large glass dewar with a stainless steel inner 6.2 l container (filled with Rn-doped LN_2). The container was surrounded by LN_2 to suppress convection. Our aim was to explain the previously observed "Rn concentration growth in time".

We have observed that the ^{214}Po collection growth in days timescale was directly caused neither by convection flows of nitrogen nor by any electrical field in the container. The electrical potential has only an influence on the Rn daughters collection efficiency on the plates immersed in LN_2, as it was shown previously.

The difference in the increase of ^{214}Po between low and high convection conditions may be explained by the mechanism of electrical charge recombination on impurities. After each decay the produced nuclide is positively charged which in electrical fields makes the nuclides mobile. The charged nuclides may be neutralized either by impurities or few free electrons.

We suppose that the content of impurities decreases in time because of freeze out on the walls of the container or sedimentation, therefore the probability of recombination becomes lower (the charged Rn daughters survival probability is higher) and the count rate rises. During the measurements we have observed that liquefying of air (impurities like O_2, CO_2, strong mixing inside the vessel) in the vessel with LN_2 and Rn increased the count rate much more than observed at other conditions. Liquefying and mixing may have an influence on the freezing out of impurities.

To explore this new results we need to perform measurements in more details. We are also preparing computer simulations of the behaviour of the nuclides in liquid nitrogen in presence of impurities.

12.4 Gamma ray screening results

From October 2008 until March 2009 the following samples have been screened for the Gerda experiment at the LNGS by means of gamma spectroscopy with HPGe detectors:

1. Coaxial cable Sami; Milano Bicocca;
2. Stainless steel of energy chains, MPIM;
3. Pins TYCO, type A; Milano Bicocca;
4. Pins ITT; Milano Bicocca;
5. Spring loaded pins MILMAX; Milano Bicocca;
6. Pins TYCO, type B; Milano Bicocca;
7. Pins TYCO, type C; Milano Bicocca;
8. PCB; Milano Bicocca;
9. FETs used for mounting on PCB; Milano Bicocca;
10. Resistors (large size) used for mounting on PCB; Milano Bicocca;

11. Capacitors NP0 used for mounting on PCB; Milano Bicocca;
12. Capacitors X5R used for mounting on PCB; Milano Bicocca;
13. Capacitor X7R used for mounting on PCB; Milano Bicocca;
14. Lead-free solder used for mounting on PCB; Milano Bicocca;
15. Resistors (small size) used for mounting on PCB; Milano Bicocca;
16. Cu rods (different diameters), MPIM;
17. EPDM used as seal for flanges of water tank; Milano Bicocca;
18. Styropor, foamable polymer, MPIK;
19. Raw copper for housing of electronics; Milano Bicocca;

The measurements regard mostly parts of the electronics that should go close to the Ge detectors (PCB, pins, cable). For the PCB a rather high ^{226}Ra contamination of $\sim$ 1 Bq/kg was detected. The bulk material of the PCB is Cuflon which was found to be very radiopure. Also the solder showed negligible ^{226}Ra contamination. Therefore, the radioactivity must have been introduced by tiny electronics components (FETs, capacitors, resisitors) which make up a total mass of not more than $\sim$ 0.1 g. To identify its origin a thorough investigation of all these components was performed. The highest levels were found for the capacitors, which have to be replaced in order to reach the specifications for the background index.

Further gamma ray screening measurements (which also included samples of the PMTs in the water Cherenkov detector) were performed in the Hades and Baksan laboratory and at MPIK.

12.5 Neutron activation measurements

Activation measurements of copper and stainless steel materials of the GERDA cryostat were performed by exposing them to cosmic rays at Gran Sasso and Heidelberg. Various radio-isotopes could be identified via low-level gamma spectrometry. As the individual cross sections for the production of radio-isotopes are poorly known and also assumptions on the cosmic ray flux must be made, additional activation measurements under well defined conditions were performed with a DT-generator at the TU Dresden, providing monoenergetic 14 MeV neutrons. This will allow the study of (n, α), (n,γ), $(n, 2n)$,(n, p) and (n, d) reactions on the materials of interest. First of all copper was activated, resulting in the expected isotopes like ^{60}Co, ^{64}Cu and ^{65}Ni. However, the observation of ^{57}Co and ^{58}Co cannot be explained by activation of copper as the neutron energy is not high enough to produce them. The only potential source of these isotopes are neutron reactions on the nickel contamination within the copper not considered before.

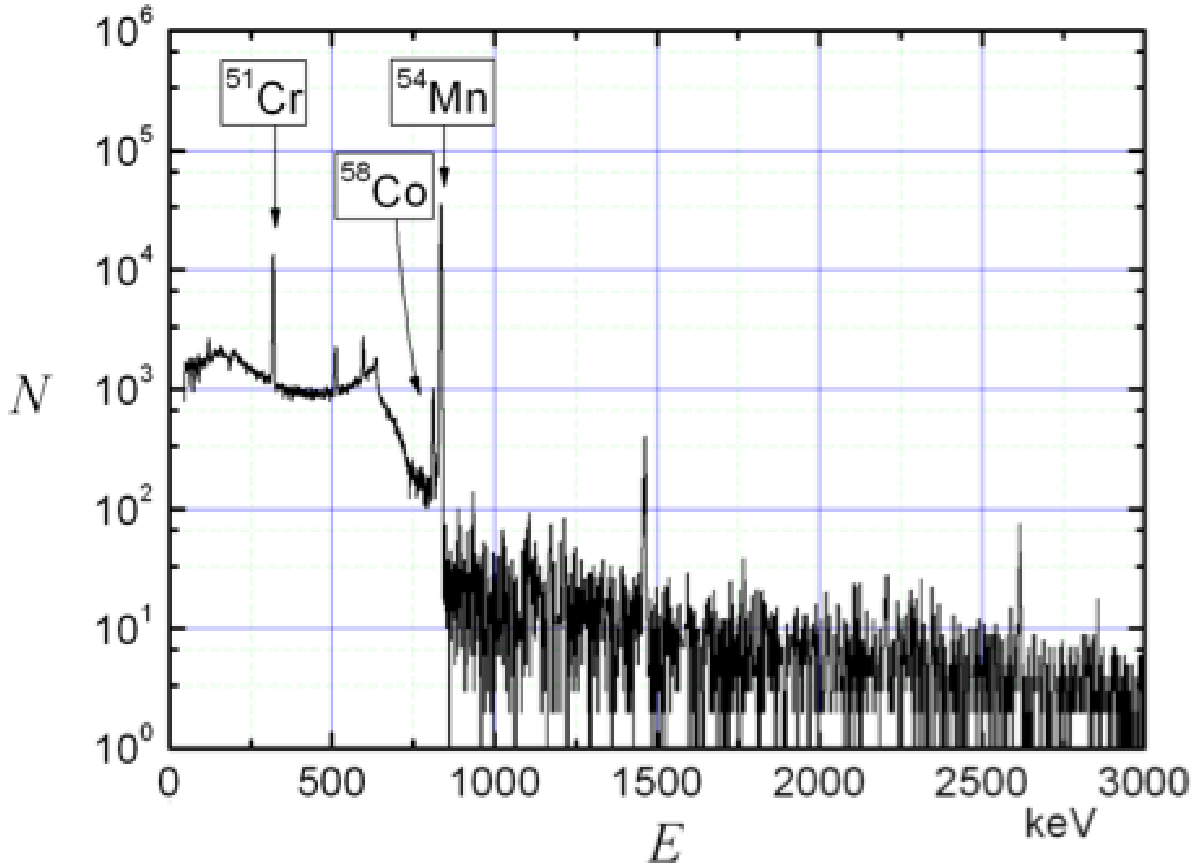

Figure 24: Energy spectrum of iron activation looking for long living activities. Clearly visible is the ^{54}Mn peak at 834.9 keV and lines from ^{51}Cr and ^{58}Co. The experimental background has not been subtracted from the spectrum.

The 1.4571 stainless steel of the GERDA cryostat contains Fe, Cr, Mo, Ni and Ti as potential sources of radionuclides. To disentangle individual contributions Fe, Mo, Ni and Ti were activated with 14 MeV neutrons individually, Cr and a sample of 1.4571 stainless steel will be done in the near future. The activation of iron shows a strong contribution of ^{54}Mn (see Fig. 24), its creation typically attributed to the reactions ^{56}Fe(n,p2n)^{54}Mn and ^{56}Fe(μ, ν 2n)^{54}Mn. However, none of these reactions can contribute to the signal observed here. The only candidate for production at 14 MeV is the ^{54}Fe(n,p)^{54}Mn reaction, normally ignored due to the relatively low natural abundance of ^{54}Fe. Looking up cross section estimates at available data bases combined with the fact that the atmospheric neutron flux is higher at lower energies it turns out that the ^{54}Fe(n,p)^{54}Mn reaction can contribute roughly 30 % to the ^{54}Mn production with respect to the considered reactions on ^{56}Fe and thus cannot be neglected. Detailed analyses of the obtained data are ongoing to determine the production cross sections.

References

[1] L.Pandola, K.T.Knöpfle, S.Schönert, and B.Schwingenheuer, *Background from radon emanation in the GERDA cryostat*, (2009) GSTR-09-001.

[2] *Performance and stability tests of bare high purity germanium detectors in liquid argon for the GERDA experiment* M. Barnabé Heider, PhD dissertation, Univ. Heidelberg, 2009

[3] D. Budjas, M. Barnabe Heider, O. Chkvorets, S. Schönert, and N. Khanbekov, *Pulse Shape Analysis with a Broad-Energy Germanium Detector for the GERDA experiment*, IEEE Nuclear Science Symposium, Oct 19-25, 2008, N30-382, arXiv0812.1735;

[4] *Germanium detector studies in the framework of the* GERDA *experiment*, D. Budjas, PhD dissertation, Univ. Heidelberg, 2009

[5] Hewlett Packard ProCurve Switch 2810-48G.

[6] DELL Power Edge R300, Quad Core Xeon X3323, 2.5 GHz.

[7] A.M. Bakalyarov *et al.*(GERDA Collaboration), GERDA status report to the LNGS Scientific Committee (November 2008), LNGS-EXP 33/08 add. 7/08

[8] M. Bauer *et al.*, Journ. of Phys., Conf. Series **39** (2006) 362; Y.-D. Chan *et al.*, arXiv:0802.0860

[9] H.V. Klapdor-Kleingrothaus *et al.*, Phys. Lett. B **586** (2004) 198

[10] I. Barabanov *et al.*, *Shielding of the GERDA experiment against external gamma background*, Nucl. Instrum. Meth. A, DOI 10.1016/j.nima.2009.04.006, in print;